# High-Accuracy Multiscale Simulation of Three-Dimensional Squeezing Carbon Nanotube-Based Flow inside a Rotating Stretching Channel

*Research Article*

# High-Accuracy Multiscale Simulation of Three-Dimensional Squeezing Carbon Nanotube-Based Flow inside a Rotating Stretching Channel

**S. Hadi Seyedi,[1] Behzad Nemati Saray,[2] and Ali Ramazani [3]**

[1]*Department of Mechanical Engineering, Wayne State University, 5050 Anthony Wayne Drive, Detroit, MI 48202, USA*
[2]*Department of Mathematics, Institute for Advanced Studies in Basic Sciences (IASBS), Zanjan 45137-66731, Iran*
[3]*Department of Mechanical Engineering, Massachusetts Institute of Technology, 77 Massachusetts Ave, Cambridge, MA 02139, USA*

Correspondence should be addressed to Ali Ramazani; ramazani@mit.edu

Received 30 April 2019; Accepted 24 July 2019; Published 26 August 2019

Academic Editor: Xiao-Qiao He



Enhancing the heat transfer rate using nanofluids is of great interest to engineers and scientists. This research aims to study the heat and mass transfer analysis of three-dimensional squeezing carbon nanotube- (CNT-) based nanofluid flow inside a rotating stretching channel. The upper wall of the channel is assumed to have a reciprocating movement, and the lower wall is assumed to be stationary and permeable. Also, radiative effects are taken into account using the Taylor series approximation. The momentum and energy equations are transformed into a coupled system of nonlinear ordinary differential equations utilizing similarity solutions. A new multiscale and accurate method was developed to solve the achieved nonlinear systems of equations. Water is chosen as the base fluid; single-wall carbon nanotubes (SWCNTs) and multiwall carbon nanotubes (MWCNTs) are added to it, and then two types of nanofluids were created. The effect of different variables such as the concentration of nanotubes, nanotube's type, suction parameter, rotation parameter, squeezing number, Eckert number, and radiation parameter on the velocity and temperature profiles is investigated. Our results reveal that the temperature profile is an increasing function of the squeezing number, suction, rotation, and radiation parameters when the upper wall moves towards the lower one.

## 1. Introduction

Fluid squeezing is a process in which two boundaries approach each other and pressurize the trapped flow between them. This process has numerous applications in science and industry such as hydraulic systems, manufacturing of fibers and papers, lubrication of bearings, cooling systems, and biomedical engineering [1]. Wang was the first one who developed squeezing flow between parallel plates in 1976 [2]. After him, Hamza and Macdonald [3] used a finite difference solution to study the two-dimensional squeezed flow in 1981. Later on, a study of magnetohydrodynamic and moving boundaries effect on a squeezed fluid film was done [4, 5]. Islam et al. analyzed the squeezing fluid flow in a porous medium channel [6], and Sherwood studied squeezing flow in the gap between non-parallel circular plates [7]. By the advent of nanotechnology and its pervasive influence in all aspects of engineering, nanofluid and its remarkable features in enhanced heat transfer were introduced by Choi and Eastman [8]. Accordingly, scholars studied the effect of adding nanoparticles to different base fluids both numerically and experimentally [9–16]. One of the most important cases that has several engineering applications is the nanofluid flow between the two walls. In our previous studies, we analyzed the heat transfer enhancement between two vertical flat plates (stationary and moving) by a high precision multiscale approach based on the Galerkin method [17–19]. Adding copper and silver nanoparticles to the base fluid helped to increase the heat transfer rate. Dib et al. [20] investigated the squeezing nanofluid flow by the Adomian decomposition method (ADM). They found out that the type of nanofluid plays an important role in heat transfer enhancement. Gupta and Saha Ray [21] developed a numerical method based on Chebyshev wavelet expansion and concluded that the Nusselt number has a direct relationship with the concentration of the

nanoparticles when the fluid is squeezing. Effect of changing the base fluid was studied in [22] for the copper nanoparticles by variation of the parameters method (VPM). Xue [23] proposed a model for thermal conductivity of carbon nanotube (CNT) composites which provide higher thermal conductivity than conventional nanoparticles such as aluminium oxide, titanium oxide, and silver. The study of squeezing nanofluid flow in a rotating channel and a lower stretching porous wall was done in [24, 25] for different nanoparticles in water. Khan et al. [26] simulated the same mentioned case by use of the Runge–Kutta–Fehlberg (RKF) method for CNTs. Ghadikolaei et al. [27, 28] investigated it with the nanofluid flow of $Fe_3O_4$ – Ag and CNTs in ethylene glycol as base fluid.

One of the best methods to solve differential equations is the Galerkin method. The Galerkin method is based on minimizing the residual with respect to the functional basis. There are some improvement methods over the standard Galerkin method; the wavelet Galerkin method (WGM) is one of the most appealing and powerful ones, thanks to the special features of the wavelet basis. One of the notable characteristics of the wavelet functions is their multiresolution analysis (MRA), and this capability provides a multiscale solution when these functions are used as a basis. On the contrary, most of the science and engineering problems are multiscale in nature and using multiscale methods in the simulation will help to a better understanding of the physics behind them.

The aspiration of the current analysis is to study the three-dimensional squeezing nanofluid flow (CNTs in water) in a rotating channel with a lower permeable stretching wall by considering radiation heat transfer effect in different scales. To do so, a robust Galerkin-based multiscale method implemented. Our proposed method in this study can provide an initial coarse solution to save time and computational resources, and accordingly, the initial coarse answer can be improved by solving the problem in the higher scales. To the best of our knowledge, there is no data for the mentioned problem. To fill out the gap in the literature, we used a novel, precise, and multiscale method for the numerical simulation of the mentioned problem.

## 2. Problem Description

An unsteady three-dimensional CNT-based nanofluid flow inside a rotating channel with a lower wall in stretching and permeable mode was considered. The lower plate of the channel is located at $y = 0$ and is stretching in only the $x$ direction with a velocity of $u = U_w = ax/(1 - ct)$. The permeation velocity at the lower wall is $-V_0/(1 - ct)$. The upper wall is assumed to have a reciprocating movement and squeezes the nanofluid with the velocity of $V_h$. Figure 1 shows the schematic of the problem. We assumed that the fluid and nanotubes are incompressible and are trapped between the two infinite horizontal plates, no chemical reaction takes place between them, there is a thermal equilibrium between the particles and base fluid, the CNTs are suspended in the base fluid, and the no-slip condition occurs between them. Single-wall carbon nanotubes (SWCNTs) and the multiwall carbon nanotubes (MWCNTs) are considered in this study.

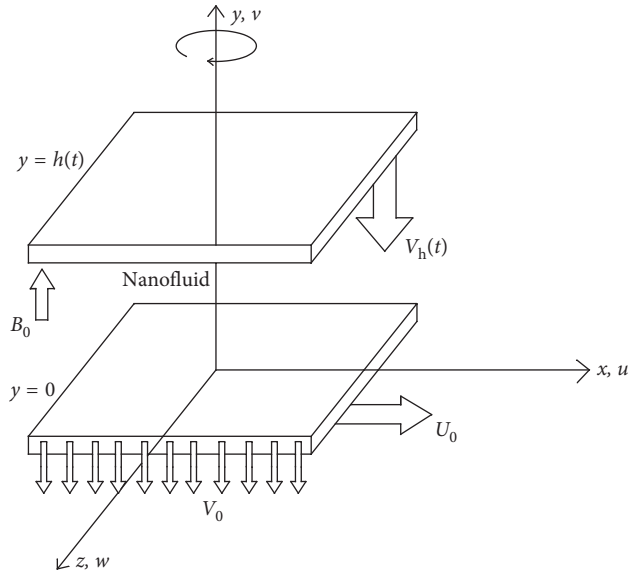


Figure 1: Geometry of the problem: nanofluid in a rotating stretching channel.

The relationship between a flow's kinetic energy and the boundary layer enthalpy difference can be described by the use of the Eckert number (Ec), which is a dimensionless number. In our problem, Ec would be showing the heat dissipation effect. Friction in the shear layer at high Eckert numbers will generate heat and will be addressed by the viscous dissipation effect. Pure water was chosen as base fluid, and then SWCNTs and MWCNTs were added to it as nanoparticles. Thermophysical properties of the base fluid and nanoparticles are tabulated in Table 1.

Considering the mentioned conditions and assumptions, the continuity, momentum, and energy equations are as follows:

$$\frac{\partial u}{\partial x} + \frac{\partial v}{\partial y} = 0, \tag{1}$$

$$\frac{\partial u}{\partial t} + u\frac{\partial u}{\partial x} + v\frac{\partial u}{\partial y} + \frac{2\omega_0}{1 - ct}w = -\frac{1}{\rho_{nf}}\frac{\partial P}{\partial x} + \frac{\mu_{nf}}{\rho_{nf}}\left(\frac{\partial^2 u}{\partial x^2} + \frac{\partial^2 u}{\partial y^2}\right), \tag{2}$$

$$\frac{\partial v}{\partial t} + u\frac{\partial v}{\partial x} + v\frac{\partial v}{\partial y} = -\frac{1}{\rho_{nf}}\frac{\partial P}{\partial y} + \frac{\mu_{nf}}{\rho_{nf}}\left(\frac{\partial^2 v}{\partial x^2} + \frac{\partial^2 v}{\partial y^2}\right), \tag{3}$$

$$\frac{\partial w}{\partial t} + u\frac{\partial w}{\partial x} + v\frac{\partial w}{\partial y} - \frac{2\omega_0}{1 - ct}w = \frac{\mu_{nf}}{\rho_{nf}}\left(\frac{\partial^2 w}{\partial x^2} + \frac{\partial^2 w}{\partial y^2}\right), \tag{4}$$

$$\begin{aligned}\frac{\partial T}{\partial t} + u\frac{\partial T}{\partial x} + v\frac{\partial T}{\partial y} - \frac{1}{(\rho C_p)_{nf}}\frac{\partial q_r}{\partial y} &= \frac{\mu_{nf}}{(\rho C_p)_{nf}}\left(\frac{\partial^2 T}{\partial x^2} + \frac{\partial^2 T}{\partial y^2}\right) + \frac{\mu_{nf}}{(\rho C_p)_{nf}}\left(4\left(\frac{\partial u}{\partial x}\right)^2\right. \\ &\left. + \left(\frac{\partial u}{\partial x} + \frac{\partial v}{\partial y}\right) + \left(\frac{\partial w}{\partial x}\right)^2 + \left(\frac{\partial w}{\partial y}\right)^2\right),\end{aligned} \tag{5}$$

Table 1: Thermophysical properties of base fluid and carbon nanotubes [26].

| Physical properties | Base fluid | SWCNT | MWCNT |
|---|---|---|---|
| $C_p$ (J/kg K) | 4179 | 425 | 796 |
| $\rho$ (kg/m$^3$) | 997.1 | 2600 | 1600 |
| $K$ (W/mK) | 0.613 | 6600 | 3000 |

where $u$, $v$, and $w$ denote the velocity in the $x$, $y$ and $z$ directions, respectively. $T$, $p$, $\rho_{nf}$, $\mu_{nf}$, $(\rho C_p)_{nf}$, and $q_r$ represent the temperature, pressure, effective density, effective dynamic viscosity, effective heat capacity, and radiative heat flux fluid for the nanofluid, respectively. The Rosseland approximation for the optically thick media can be used:

$$q_r = \frac{-4\sigma^*}{3k^*}\left(\frac{\partial T^4}{\partial y}\right), \tag{6}$$

where $\sigma^*$ and $k^*$ are showing the Stefan–Boltzman constant and Rosseland mean spectral absorption coefficient, respectively. We assume that there is a small temperature difference in the flow and by use of Taylor series approximation about the temperature $T_0$, we have

$$T^4 \approx 4T_0^3 T - 3T_0^4. \tag{7}$$

By replacing equations (6) and (7) in equation (5), we have

$$\frac{\partial T}{\partial t} + u\frac{\partial T}{\partial x} + v\frac{\partial T}{\partial y} - \frac{1}{(\rho C_p)_{nf}}\frac{16T_h^3\sigma^*}{3k^*}\frac{\partial}{\partial y}\left(\frac{\partial T}{\partial y}\right) = \frac{\mu_{nf}}{(\rho C_p)_{nf}}\left(\frac{\partial^2 T}{\partial x^2} + \frac{\partial^2 T}{\partial y^2}\right) + \frac{\mu_{nf}}{(\rho C_p)_{nf}} \left(4\left(\frac{\partial u}{\partial x}\right)^2 + \left(\frac{\partial u}{\partial x} + \frac{\partial v}{\partial y}\right) + \left(\frac{\partial w}{\partial x}\right)^2 + \left(\frac{\partial w}{\partial y}\right)^2\right). \tag{8}$$

The relative boundary conditions are

$$\begin{aligned} u &= U_w = \frac{ax}{1-ct}, \\ v &= \frac{-V_0}{1-ct}, \\ w &= 0, \\ T &= T_w \text{ at } y = 0, \\ u &= 0, \\ v &= V_h = \frac{-c}{2}\sqrt{\frac{\nu}{a(1-ct)}}, \\ w &= 0, \\ T &= T_h \text{ at } y = h(t). \end{aligned} \tag{9}$$

where $a > 0$ means the lower wall of the channel is stretching. The nanofluid effective density and heat capacities are defined by

$$A_1 = (1-\phi) + \phi\frac{\rho_{CNT}}{\rho_f}, \tag{10}$$

$$A_2 = (1-\phi) + \phi\frac{(\rho C_p)_{CNT}}{(\rho C_p)_f}. \tag{11}$$

For effective dynamic viscosity of nanofluid, we use the approximation given by Brinkman [29] for spherical particles:

$$\mu_{nf} = \frac{\mu_f}{(1-\phi)^{2.5}}. \tag{12}$$

Effective thermal conductivity can be characterized by the use of different approximations. In this project, we used the model presented by Xue [23] for the carbon nanotubes:

$$A_3 = \frac{K_{nf}}{K_f} = \frac{(1-\phi) + 2\phi(k_{CNT}/(k_{CNT}-k_f))\ln((k_{CNT}+k_f)/2k_f)}{(1-\phi) + 2\phi(k_f/(k_{CNT}-k_f))\ln((k_{CNT}+k_f)/2k_f)}, \tag{13}$$

where $\phi$ is the volume fraction of nanoparticles and $k_{CNT}$ is showing the thermal conductivity of the carbon nanotubes.

For simplifying the governing equations to a nondimensional set of ordinary differential equations (ODEs), the following transformations are given:

$$\begin{aligned} \eta &= \frac{y}{h(t)}, \\ u &= U_w f'(\eta), \\ v &= \sqrt{\frac{a\nu}{a(1-ct)}} f(\eta), \\ \theta(\eta) &= \frac{T - T_w}{T_w - T_h}, \\ w &= U_W g(\eta), \end{aligned} \tag{14}$$

where $\eta$ is the local similarity variable, $f(\eta)$ and $f'(\eta)$ represent the velocity along the $y$ and $x$ axes, and $g(\eta)$ and $\theta(\eta)$ correspond to the rotational velocity and temperature profile, respectively.

By using and substituting equation (14) in equations (1)–(4) and considering equations (8)–(13), we have

$$f^{iv} - A_1(1-\phi)^{2.5}\left(2\Omega g' - ff''' + f'f'' + \frac{S}{2}\left(3f'' + \eta f'''\right)\right) = 0,$$

$$g'' + A_1(1-\phi)^{2.5}\left(2\Omega f' - gf' + g'f - S\left(g + \frac{\eta}{2}g'\right)\right) = 0, \tag{15}$$

$$\left(1 + \frac{R}{A_3}\right)\theta'' + \left(\Pr\frac{A_2}{A_3}\right)\left(f'\theta - \frac{S}{2}\eta\theta'\right) + \frac{\Pr A_2}{A_3(1-\phi)^{2.5}}\left(\mathrm{Ec}\left(4f^2 + g^2\right) + \mathrm{Ec}_x\left(\left(f''\right)^2 + \left(f'\right)^2\right)\right) = 0.$$

The coefficient $(1-\phi)^{2.5}$ originated from approximation given by Brinkman in equation (7).

Similar transforms change the boundary conditions of the problem to a more simplified form:

$$\begin{aligned} f(0) &= A, \\ f'(0) &= 1, \\ g(0) &= 0, \\ \theta(0) &= 1, \\ f(1) &= \frac{S}{2}, \\ f'(1) &= 0, \\ g(1) &= 0, \\ \theta(1) &= 0. \end{aligned} \tag{16}$$

The nondimensional variables in the above equations are defined as follows:

$$\begin{aligned} \Omega &= \frac{\omega_0}{a}, \\ \mathrm{Ec} &= \frac{\nu^2}{h^2\left(C_\mathrm{p}\right)_\mathrm{f}\left(T_w - T_\mathrm{h}\right)}, \\ \Pr &= \frac{\mu_\mathrm{f}\left(C_\mathrm{p}\right)_\mathrm{f}}{k_\mathrm{f}}, \\ S &= \frac{c}{a}, \\ A &= \frac{V_0}{ah}, \\ \mathrm{Ec}_x &= \frac{U_w^2}{\left(C_\mathrm{p}\right)_\mathrm{f}\left(T_w - T_\mathrm{h}\right)}, \\ R &= \frac{16T_\mathrm{h}^3\sigma^\star}{3k^\star k_\mathrm{f}}, \end{aligned} \tag{17}$$

where $\Omega$ is the rotational parameter; $A$ is the suction parameter; $S$ is the squeezing number, and positive one means the upper wall is moving toward the lower stationary one (and vice versa); Pr is the Prandtl number; Ec is the Eckert number; $\mathrm{Ec}_x$ is the modified Eckert number; and $R$ is the radiation parameter. When there is no movement in the upper wall ($S = 0$), the unsteady flow will turn to a steady flow. We are using the definition of [28] for defining the Nusselt number and skin friction coefficient:

$$\begin{aligned} \mathrm{Nu}_\mathrm{lower} &= \left(\frac{X(\partial T/\partial y)}{K_\mathrm{nf}\left(T_w - T_\mathrm{h}\right)}\right)_{y=0} + q_r, \\ \mathrm{Nu}_\mathrm{upper} &= \left(\frac{X(\partial T/\partial y)}{K_\mathrm{nf}\left(T_w - T_\mathrm{h}\right)}\right)_{y=h(t)} + q_r, \\ \mathrm{Cf}_\mathrm{lower} &= \left(\frac{\mu_\mathrm{nf}(\partial u/\partial y)}{\rho_\mathrm{nf}U_0^2}\right)_{y=0}, \\ \mathrm{Cf}_\mathrm{upper} &= \left(\frac{\mu_\mathrm{nf}(\partial u/\partial y)}{\rho_\mathrm{nf}U_0^2}\right)_{y=h(t)}. \end{aligned} \tag{18}$$

Nondimensional format of the above equations can be written as follows:

$$\begin{aligned} \left(\mathrm{NuRe}_x^{-0.5}\right)_\mathrm{lower} &= -(A_3 + R)\theta'(0), \\ \left(\mathrm{NuRe}_x^{-0.5}\right)_\mathrm{upper} &= -(A_3 + R)\theta'(1), \\ \left(\mathrm{CfRe}_x^{0.5}\right)_\mathrm{lower} &= \frac{f''(0)}{A_1(1-\phi)^{2.5}}, \\ \left(\mathrm{CfRe}_x^{0.5}\right)_\mathrm{upper} &= \frac{f''(1)}{A_1(1-\phi)^{2.5}}, \end{aligned} \tag{19}$$

where the term $\mathrm{Re}_x = U_w x/\nu_\mathrm{f}$ is called the local Reynolds number.

## 3. Alpert's Multiwavelets

Alpert et al. [30, 31] introduced an orthogonal basis for $L^2(\mathbb{R})$ and $L^2([0,1])$ using multiresolution analysis (MRA). These bases are indexed by a parameter $r \geq 0$ and built based on Legendre polynomials of degree less than $r$. Over the last decade, Alpert's multiwavelets have been used in numerous

areas of mathematics, engineering, computer science, statistics, physics, etc [30, 32–35].

Let $\overline{\Omega} \coloneqq [0,1] = \cup_{b\in\mathscr{B}} I_{j,b}$, where $I_{j,b} = [x_{j,b}, x_{j,b+1}]$ and $\mathscr{B} \coloneqq \{0,1,\ldots,2^j-1\}$ for $j \in \mathbb{Z}^+\cup\{0\}$. Also, suppose that $\mathscr{D}_a$ and $\mathscr{T}_b$ are the dilation and the translation operators, respectively, such that $\mathscr{D}_a f(x) = a^{1/2} f(ax)$ and $\mathscr{T}_b f(x) = f(x-b)$.

According to the characteristics of MRA, one can introduce a set of scaling functions for subspaces $V_j^r \in L^2[0,1]$ using the dilation and the translation operators, i.e.,

$$V_j^r = \operatorname{span}\left\{\varphi_{j,b}^k \coloneqq \mathscr{D}_{2^j}\mathscr{T}_b\varphi^k, \quad b\in\mathscr{B}, k = 0,1,\ldots,r-1\right\}. \tag{20}$$

Based on the definition of this wavelets, it is obvious that $V_j^r$ is the collection of piecewise polynomials which are of degree less than $r$ on the interval $I_{j,b}$, $b \in \mathscr{B}$. As the subspaces $V_j^r$ are nested, there exist complementary orthogonal subspaces $W_j^r$ such that

$$V_{j+1}^r = V_j^r \oplus W_j^r, \quad j\in\mathbb{N}, \tag{21}$$

where $\oplus$ represents orthogonal sumations. This gives rise to an orthogonal decomposition of $L^2[0,1]$, i.e.,

$$L^2[0,1] = \bigoplus_{j\in\mathbb{N}} W_j^r. \tag{22}$$

So there exists a family of other basis that generate the complementary subspaces $W_j^r$, namely,

$$W_j^r = \operatorname{span}\left\{\psi_{j,b}^k \coloneqq \mathscr{D}_{2^j}\mathscr{T}_b\psi^k, \quad b\in\mathscr{B}, k = 0,1,\ldots,r-1\right\}. \tag{23}$$

The functions $\psi_{j,b}^k$ are called multiwavelets. In other words, from (21), the multiwavelets $\psi_{j,b}^k$, $b\in\mathscr{B}$, $k = 0,1,\ldots,r-1$, form a family of bases for the orthogonal complement space $W_j^r = V_{j+1}^r/V_j^r$. On the contrary, it can be shown that $\langle\psi_{j,b}^k, \widetilde{\psi}_{\tilde{j},\tilde{b}}^{\tilde{k}}\rangle = \delta_{j,\tilde{j}}\delta_{b,\tilde{b}}\delta_{k,\tilde{k}}$ where $\delta$ is the Kronecker delta function. Therefore, this family of basis is orthonormal with respect to the $L^2$ inner product.

Due to the fact that $V_j^r \subset V_{j+1}^r$ and $W_j^r \subset V_{j+1}^r$, vector functions $\mathbf{\Phi}_0^{r,0} \coloneqq [\varphi_{0,0}^0,\ldots,\varphi_{0,0}^{r-1}]^{\mathrm{T}}$ and $\mathbf{\Psi}_0^{r,0} \coloneqq [\psi_{0,0}^0,\ldots,\psi_{0,0}^{r-1}]^{\mathrm{T}}$ satisfy a matrix refinement equation:

$$\mathbf{\Phi}_0^{r,0}(x) = \sum_{b\in\mathscr{B}} H^b\mathscr{D}_2\mathscr{T}_b\mathbf{\Phi}_0^{r,0}(x) = \sum_{b\in\mathscr{B}} H^b\mathbf{\Phi}_1^{r,b}(x), \tag{24}$$

$$\mathbf{\Psi}_0^{r,0}(x) = \sum_{b\in\mathscr{B}} G^b\mathscr{D}_2\mathscr{T}_b\mathbf{\Phi}_0^{r,0}(x) = \sum_{b\in\mathscr{B}} G^b\mathbf{\Phi}_1^{r,b}(x), \tag{25}$$

where $\mathbf{\Phi}_j^{r,b} \coloneqq \mathscr{D}_{2^j}\mathscr{T}_b\mathbf{\Phi}_0^{r,0} = [\varphi_{j,b}^0,\ldots,\varphi_{j,b}^{r-1}]^{\mathrm{T}}$ and $H^b$ and $G^b$ for $b\in\mathscr{B}$ are $(r\times r)$ matrices with constant elements that are introduced in [30].

*3.1. Multiscale Transformation.* From (21), for a fixed integer $J \le 0$, it is easy to find multiscale decomposition $V_J^r = V_0^r \oplus (\oplus_{j=0}^{J-1} W_j^r)$. Using this decomposition, we are able to approximate any function $f\in L^2(\Omega)$ by the multiscaling functions of the coarse space $V_0^r$ and multiwavelets of the higher levels $W_j^r$, $j = 0,1,\ldots,J-1$. Now we introduce multiscale operator $\mathscr{M}_J^r$ that maps $L^2(\Omega)$ onto $V_J^r$ via

$$f \approx \mathscr{M}_J^r(f) = \left(\mathscr{P}_0^r + \sum_{j=0}^{r-1}\mathscr{Q}_j^r\right)(f), \tag{26}$$

where $\mathscr{P}_0^r$ and $\mathscr{Q}_j^r$ for $j = 0,\ldots,r-1$ are the orthonormal projection operators that map $L^2(\overline{\Omega})$ onto $V_j^r$ and $W_j^r$, respectively. The multiscale operator $\mathscr{M}_J^r$ defines the multiscale transformation, i.e.,

$$f \approx \mathscr{M}_J^r(f) = \sum_{k=0}^{r-1} f_{0,0}^k\varphi_{0,0}^k + \sum_{k=0}^{r-1}\sum_{j=0}^{J-1}\sum_{b=0}^{2^j-1}\widetilde{f}_{j,b}^k\psi_{j,b}^k, \tag{27}$$

where the coarse scale coefficients $f_{0,0}^k$ and multiwavelets coefficients $\widetilde{f}_{j,b}^k$ are determined by the orthonormal property of Alpert's multiwavelets:

$$\begin{aligned} f_{0,0}^k &\coloneqq \langle f, \varphi_{0,0}^k\rangle, \\ \widetilde{f}_{j,b}^k &\coloneqq \langle f, \psi_{j,b}^k\rangle. \end{aligned} \tag{28}$$

Assume that $\mathbf{\Psi}_J^r \coloneqq [\mathbf{\Phi}_0^{r,0^{\mathrm{T}}}, \mathbf{\Psi}_0^{r,0^{\mathrm{T}}}, \mathbf{\Psi}_0^{r,0^{\mathrm{T}}}, \ldots, \mathbf{\Phi}_J^{r,b_{\max^{\mathrm{T}}}}]^{\mathrm{T}}$ where $b_{\max} \coloneqq \max b\in\mathscr{B}$. In fact, for a fixed number $r$ and $J$, $\mathbf{\Psi}_J^r$ is a vector function that includes the scaling functions in the coarse space $V_0^r$ and the high-level spaces $W_j^r$, $j = 0,1,\ldots,J-1$. By this introduction, we are able to write

$$f \approx \mathscr{M}_J^r(f) = \widetilde{F}_J^{\mathrm{T}}\mathbf{\Psi}_J^r, \tag{29}$$

where $\widetilde{F}_J$ is an $r2^J$-dimensional vector with entries $f_{0,0}^k$ and $\widetilde{f}_{j,b}^k$ for $b\in\mathscr{B}$, $j = 0,\ldots,J-1$, and $k = 0,\ldots,r-1$.

It should be mentioned that the coefficients $f_{0,0}^k$ and $\widetilde{f}_{j,b}^k$ for $b\in\mathscr{B}$, $j = 0,\ldots,J-1$, and $k = 0,\ldots,r-1$ must be obtained to find the multiscaling transformation (27). One can calculate the single-scale coefficients, $f_{0,0}^k = 0,1,\ldots,r-1$, according to the interpolating property of interpolating scaling functions [30]. But for evaluating the multiwavelets coefficients $\widetilde{f}_{j,b}^k$, this property does not exist. One remedy for this problem is numerically calculating the integrals. To avoid this action, we introduce a new matrix that is known as the wavelet transform matrix and is obtained using two-scale refinement relations (24) and (25). In fact, the wavelet transform matrix $T_J$ helps us to obtain the multiwavelets by using the scaling functions, i.e.,

$$\mathbf{\Psi}_J^r = T_J\mathbf{\Phi}_J^r, \tag{30}$$

where $T_J$ is an $(n\times n)$ matrix which is obtained by the following scheme. Generally, the refinement equation of multiscaling functions for neighboring scales $J$ and $J+1$ is

given by $\mathbf{\Phi}_J^r = H_J \mathbf{\Phi}_{J+1}^r$ where $H_J = I_{2^J} \otimes H$, $H = [H^0 H^1]$, and $I_{2^J}$ is the identity matrix of size $2^J$. Let the vector function $\Upsilon_J^r := [\mathbf{\Psi}_j^{r,0}, \ldots, \mathbf{\Psi}_j^{r,2^j-1}]^{\mathrm{T}}$ satisfies $\Upsilon_J^r = G_J \mathbf{\Phi}_{j+1}^r$ for $j = 0, 1, \ldots, J-1$ where $G_J = I_{2^J} \otimes G$ and $G = [G^0 G^1]$. Now we are able to determine the wavelet transform matrix as

$$T_J = \begin{bmatrix} \frac{1}{2^J}\left(H_0 \times H_1 \times \cdots \times H_{J-1}\right) \\ \\ \frac{1}{2^J}\left(G_0 \times H_1 \times \cdots \times H_{J-1}\right) \\ \\ \frac{1}{2^{J-1}}\left(G_1 \times H_2 \times \cdots \times H_{J-1}\right) \\ \\ \vdots \\ \\ \frac{1}{2^2}\left(G_{J-2} \times H_{J-1}\right) \\ \\ \frac{1}{2} G_{J-1} \end{bmatrix}. \tag{31}$$

One can compute the elements of matrices $G^0$, $G^1$, $H^0$, and $H^1$ easily using the interpolation property and orthonormality of Alpert's multiwavelets [30]. There is also a reconstruction formula [30]:

$$\mathbf{\Phi}_1^{r,b} = \overline{G}^b \mathbf{\Psi}_0^r + \overline{H}^b \mathbf{\Phi}_0^r, \quad b = 0, 1. \tag{32}$$

Relations (24), (25), and (32) yield algorithms for the transition between different scales of the multiresolution analysis.

## 4. Wavelet Galerkin Method (WGM)

Wavelet Galerkin methods (WGM) provides an approximated solution to the differential equations by the formalism to generate discrete algorithms. Let us write the largest derivative of the unknown solution of equation (15) in terms of the basis of $V_J^r \in L^2[0,1]$. Let $u^{(N)} \approx \mathscr{M}_J^r(u^{(N)}) = U^{\mathrm{T}} \mathbf{\Psi}_J^r$; by successive integration from both sides of this equation and using the operational matrix of integration $I_\psi$ which is introduced in [18, 33], we can write

$$u^{(N-m)}(\eta) \approx U^{\mathrm{T}} I_{\mathbf{\Psi}}^m \mathbf{\Psi}_J^r(\eta) + \sum_{i=1}^{m} u^{(N-i)}(0) \frac{\eta^{m-i}}{(m-i)!}, \quad m = 0, \ldots, N, \tag{33}$$

where super index $N$ has been used for the largest derivatives and $u^{(N-i)}(0)$ for $i = 1, 2, \ldots, m$ is a known constant determined by boundary conditions. To use the wavelet Galerkin method, we expand $u^{(N-i)}(0)(\eta^{m-i}/(m-i)!)$ using Alpert's multiwavelets:

$$u^{(N-i)}(0) \frac{\eta^{m-i}}{(m-i)!} = \Lambda_{m,i}^{\mathrm{T}} \mathbf{\Psi}_J^r(\eta), \quad i = 1, \ldots, m. \tag{34}$$

According to (33) and (34), we have

$$u^{(N-m)}(\eta) \approx U^{\mathrm{T}} I_\psi^m \mathbf{\Psi}_J^r(\eta) + \sum_{i=1}^{m} \Lambda_{m,i}^{\mathrm{T}} \mathbf{\Psi}_J^r(\eta). \tag{35}$$

In the same way, we can find the closed form for $f$, $g$, and $\theta$ and their derivatives, namely,

$$\begin{aligned} f^{(N-m)}(\eta) &\approx F^{\mathrm{T}} I_\psi^m \mathbf{\Psi}_J^r(\eta) + \sum_{i=1}^{m} \Lambda_{1_{m,i}^T} \mathbf{\Psi}_J^r(\eta), \\ g^{(N-m)}(\eta) &\approx G^{\mathrm{T}} I_\psi^m \mathbf{\Psi}_J^r(\eta) + \sum_{i=1}^{m} \Lambda_{2_{m,i}^T} \mathbf{\Psi}_J^r(\eta), \\ \theta^{(N-m)}(\eta) &\approx \Theta^{\mathrm{T}} I_\psi^m \mathbf{\Psi}_J^r(\eta) + \sum_{i=1}^{m} \Lambda_{3_{m,i}^T} \mathbf{\Psi}_J^r(\eta). \end{aligned} \tag{36}$$

Using wavelet transform matrix $T_J$ and interpolating property of this type of wavelets, we can approximate the nonlinear terms of (15) as

$$\begin{aligned} \mathscr{M}_J^r(f f''')(\eta) &= P_1^{\mathrm{T}} \mathbf{\Psi}_J^r(\eta), \\ \mathscr{M}_J^r(f' f'')(\eta) &= P_2^{\mathrm{T}} \mathbf{\Psi}_J^r(\eta), \\ \mathscr{M}_J^r(g f')(\eta) &= P_3^{\mathrm{T}} \mathbf{\Psi}_J^r(\eta), \\ \mathscr{M}_J^r(g' f)(\eta) &= P_4^{\mathrm{T}} \mathbf{\Psi}_J^r(\eta), \\ \mathscr{M}_J^r(f' \theta)(\eta) &= P_5^{\mathrm{T}} \mathbf{\Psi}_J^r(\eta), \\ \mathscr{M}_J^r\left(f^2\right)(\eta) &= P_6^{\mathrm{T}} \mathbf{\Psi}_J^r(\eta), \\ \mathscr{M}_J^r\left(g^2\right)(\eta) &= P_7^{\mathrm{T}} \mathbf{\Psi}_J^r(\eta), \\ \mathscr{M}_J^r\left(f'^2\right)(\eta) &= P_8^{\mathrm{T}} \mathbf{\Psi}_J^r(\eta), \\ \mathscr{M}_J^r\left(g'^2\right)(\eta) &= P_9^{\mathrm{T}} \mathbf{\Psi}_J^r(\eta). \end{aligned} \tag{37}$$

We can also expand the functions $\eta f'''$, $\eta \theta'$, and $\eta g'$ in the same way:

$$\begin{aligned} \mathscr{M}_J^r(\eta f''')(\eta) &= P_{10}^{\mathrm{T}} \mathbf{\Psi}_J^r(\eta), \\ \mathscr{M}_J^r(\eta g')(\eta) &= P_{11}^{\mathrm{T}} \mathbf{\Psi}_J^r(\eta), \\ \mathscr{M}_J^r(\eta \theta')(\eta) &= P_{12}^{\mathrm{T}} \mathbf{\Psi}_J^r(\eta), \end{aligned} \tag{38}$$

where $P_i$ for $i = 1, \ldots, 12$ are the $r2^J \times 1$ vectors. Let us to look back into equation (15). Using equations (36)–(38), we have

Table 2: Comparison of numerical values for $f''(0)$ and $g'(0)$ between the different methods taking $r = 6$ and $J = 2$.

| | | | RK method [36] | | Proposed method ($r = 6, J = 2$) | |
|---|---|---|---|---|---|---|
| $\Omega$ | $A$ | $S$ | $f''(0)$ | $g'(0)$ | $f''(0)$ | $g'(0)$ |
| 0.5 | 0.5 | 0.0 | −7.419696 | −0.237555 | −7.419696 | −0.237555 |
| | | 1.0 | −4.445146 | 0.075782 | −4.445146 | 0.075782 |
| | | 2.0 | −1.297045 | 0.300313 | −1.297045 | 0.300313 |
| | | 3.0 | 2.018006 | 0.469820 | 2.018006 | 0.469820 |
| | 0.3 | 2.0 | 0.025724 | 0.372682 | 0.025724 | 0.372682 |
| | 0.5 | | −1.297045 | 0.300313 | −1.297045 | 0.300313 |
| 0.5 | 0.8 | | −3.369658 | 0.172293 | −3.369658 | 0.172293 |
| | 1.0 | | −4.814071 | 0.072293 | −4.814071 | 0.072293 |
| | 1.2 | | −6.311701 | −0.040879 | −6.311701 | −0.040879 |
| 1.0 | 0.5 | 2 | −1.291472 | 0.600474 | −1.291472 | 0.600474 |
| 3.0 | | | −1.231657 | 1.796681 | −1.231657 | 1.796681 |
| 5.0 | | | −1.110254 | 2.979537 | −1.110254 | 2.979539 |
| 7.0 | | | −0.924676 | 4.142754 | −0.924676 | 4.142759 |
| 10.0 | | | −0.522086 | 5.844396 | −0.522085 | 5.844413 |

$$\begin{aligned}
&\left(F^{\mathrm{T}} - A_1(1-\phi)^{2.5}\left(2\Omega\left(G^{\mathrm{T}} I_{\Psi} + \Lambda^{\mathrm{T}}_{21,1}\right) - P^{\mathrm{T}}_1 + P^{\mathrm{T}}_2 + \frac{S}{2}\left(3F^{\mathrm{T}} + \Lambda^{\mathrm{T}}_{12,1} + \Lambda^{\mathrm{T}}_{12,2} + P^{\mathrm{T}}_{10}\right)\right)\right)\boldsymbol{\Psi}^r_J(\eta) = 0,\\
&\left(G^{\mathrm{T}} + A_1(1-\phi)^{2.5}\left(2\Omega\left(F^T I^3_{\Psi} + \sum_{i=1}^{3}\Lambda^{\mathrm{T}}_{13,i}\right) - P^{\mathrm{T}}_3 + P^{\mathrm{T}}_4 - S\left(G^{\mathrm{T}} I^2_{\Psi} + \sum_{i=1}^{2}\Lambda^{\mathrm{T}}_{22,i} + P^{\mathrm{T}}_{11}\right)\right)\right)\boldsymbol{\Psi}^r_J(\eta) = 0,\\
&\left(1 + \frac{R}{A_3}\Theta^{\mathrm{T}} + \left(\mathrm{Pr}\frac{A_2}{A_3}\right)\left(P^{\mathrm{T}}_5 - \frac{S}{2}P^{\mathrm{T}}_{12}\right) + \frac{\mathrm{Pr}A_2}{A_3(1-\phi)^{2.5}}\left(\mathrm{Ec}\left(4P^{\mathrm{T}}_6 + P^{\mathrm{T}}_7\right) + \mathrm{Ec}_x\left(P^{\mathrm{T}}_8 + P^{\mathrm{T}}_9\right)\right)\right)\boldsymbol{\Psi}^r_J(\eta) = 0.
\end{aligned} \tag{39}$$

Applying the Wavelet Galerkin method (multiplying both side in $\boldsymbol{\Psi}^r_J(\eta)$ and integrating over $\overline{\Omega}$), we get a system of nonlinear algebraic equations that we solve it using the Newton method to find the unknown coefficients and numerical solutions.

## 5. Results and Discussion

Implementation of the discussed method on the obtained governing equations provides an analysis of each input parameters effect. To show the multiscale solution for the problem and as an accuracy test, Table 2 and Figure 2 are provided. As it can be seen, results are shown in different scale levels ($J$) and by using different orders of polynomials ($r$) in comparison to the reference method, fourth-order Runge–Kutta (RK method). Increasing the order of polynomials and scale levels should help to converge the results to the precise answer. Table 2 represents the accuracy of the proposed method. One can see that, by using the sixth order polynomials and just in the second-scale level, the WGM method can provide results with very high accuracy, and Figure 2 shows the effect of increasing the $J$ and $r$ values on the $L_2$ error for $f''(0)$ and $g'(0)$ in the logarithmic scale.

Effect of the concentration of nanoparticles $\phi$ on the heat transfer and velocity profiles is one of the most important surveys in any nanofluid study. For our case, pure water was chosen as the base fluid, and then two carbon nanotubes with different thermophysical properties, which are depicted in Table 1, were added to it. We increased the amount of $\phi$, and Figure 3 shows this effect on the velocity and temperature profiles. It can be seen in Figure 3(a) that there is a direct relationship between the nanoparticle volume fraction and the velocity in the $y$ direction ($f(\eta)$) for both single- and multi-wall carbon nanotubes; also, this effect is more remarkable in the first half of the channel. In Figure 3(b), one can see that when $\eta$ is between zero and 0.35, by increasing the nanoparticle concentration, we will have higher velocity in the $x$ direction; however, for the rest of the $\eta$ values, there is an opposite trend for velocity ($f'(\eta)$). Figure 3(c) depicts the behavior of rotational velocity by increasing the nanoparticle volume fraction. One can see a reverse flow in the center of the channel. It is possible to reduce the mentioned reverse flow by adding more nanotubes to the water. One important point about the discussed figure is that, in higher concentrations, the MWCNT's rotational velocity will change more than SWCNT's velocity. The physical reason can be related to the fact of lower densities for SWCNTs. Effect of volume fraction on temperature profiles can be found in Figure 3(d), and the opposite trend of temperature profiles with $\phi$ is obvious. By adding more nanoparticles to the base fluid, the higher thermal conductivity of the nanoparticles causes an increase in the heat transfer. Accordingly, temperature profiles will drop (Figure 3(d)). By zooming in on the temperature profile, we can see higher values of $\theta$ for the MWCNTs which is due to lower thermal conductivity of these types of particles. Another important conclusion from the temperature profiles is that when we compare the differences in heat transfer amount between the pure water and 10 percent nanofluid, we see a huge difference. However, adding more

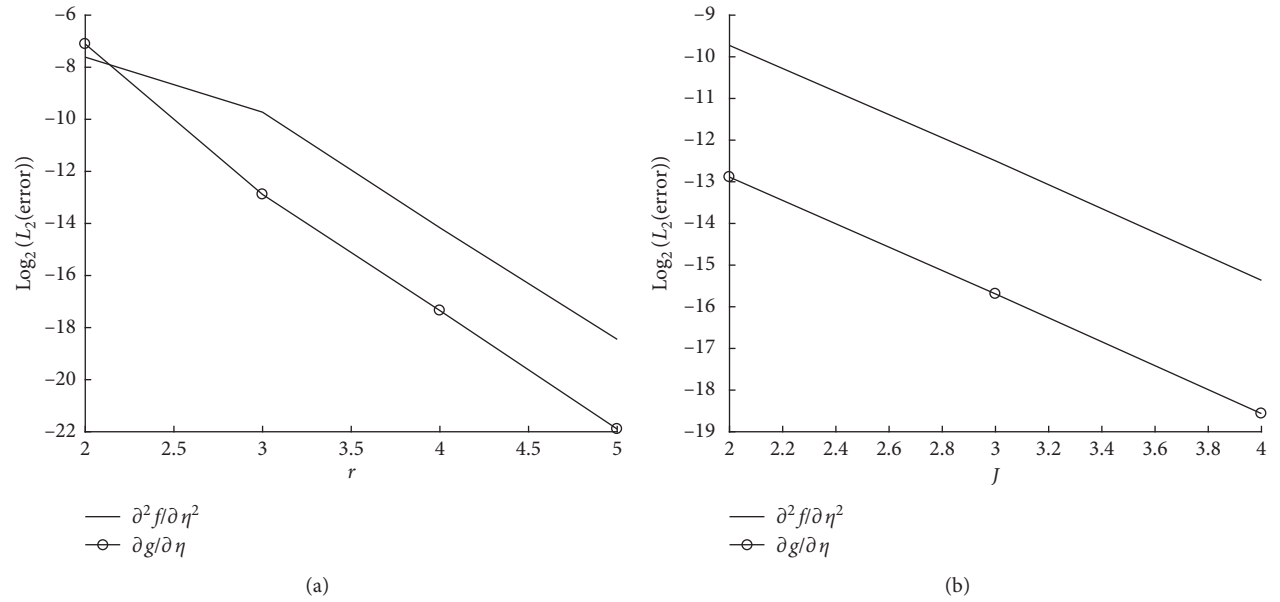


Figure 2: Effect of parameters $J$ and $r$ on the $L_2$ error.

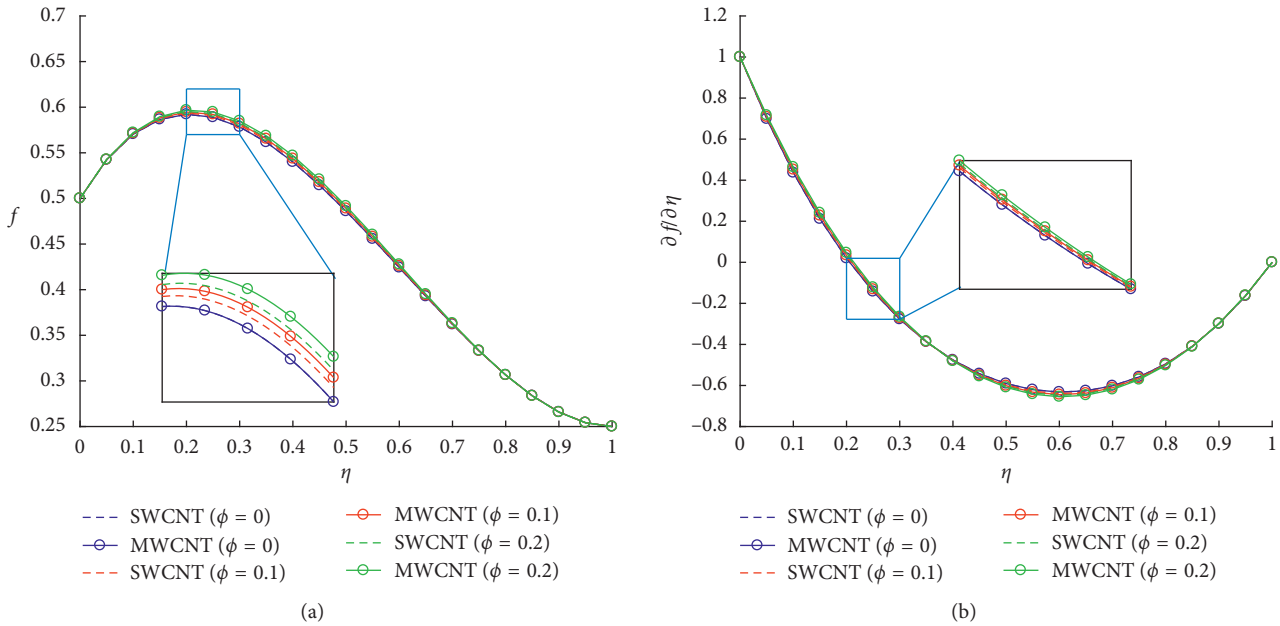


Figure 3: Continued.

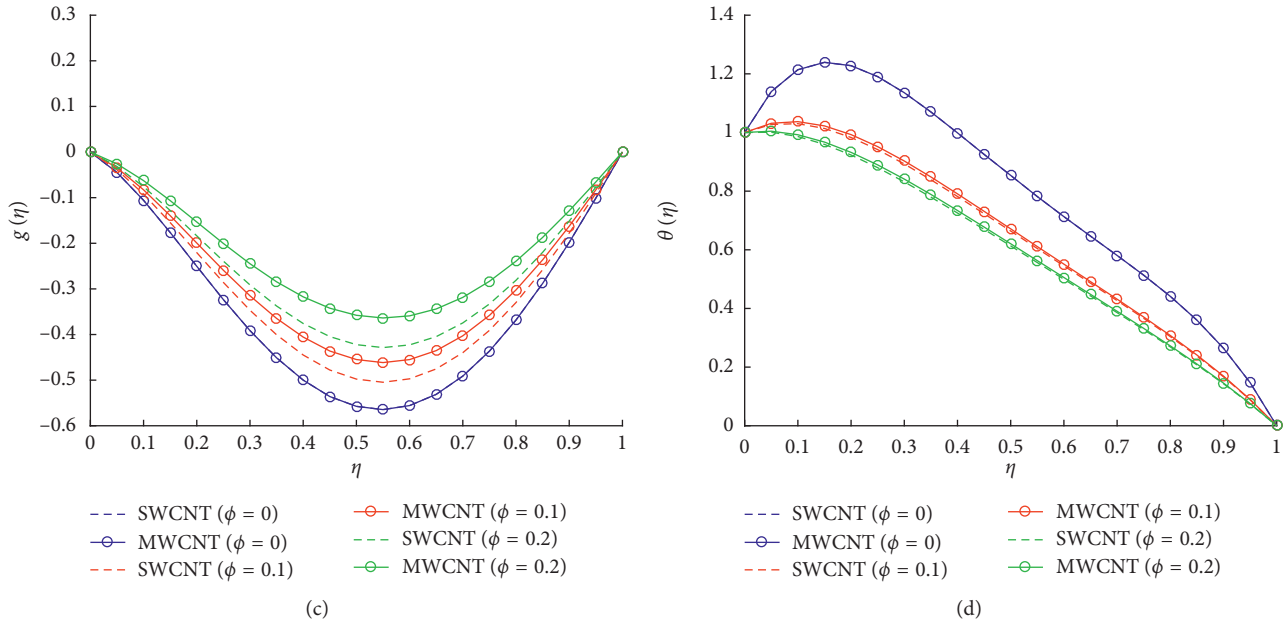


FIGURE 3: Effects of the nanoparticle volume fraction on the velocity and temperature profiles when $\Omega = 5$, $\mathrm{Ec} = \mathrm{Ec}_x = 0.1$, $\mathrm{Pr} = 6.2$, $A = S = 0.5$, and $R = 0$, taking $r = 5$ and $J = 2$.

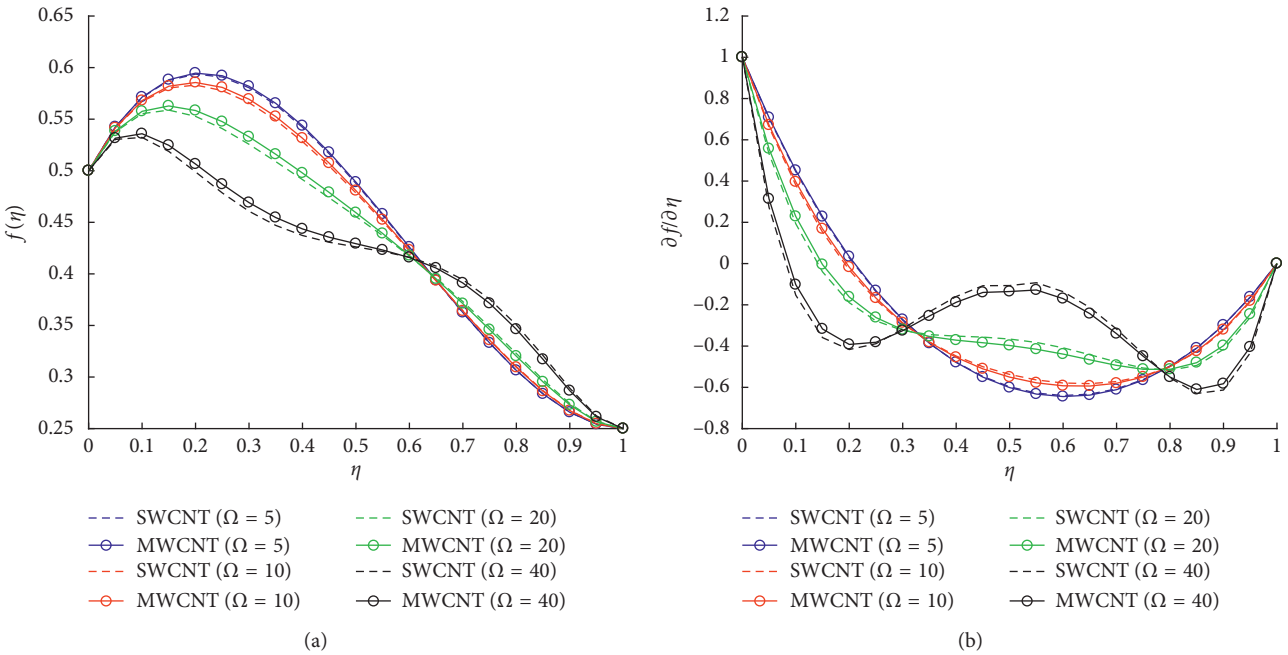


FIGURE 4: Continued.

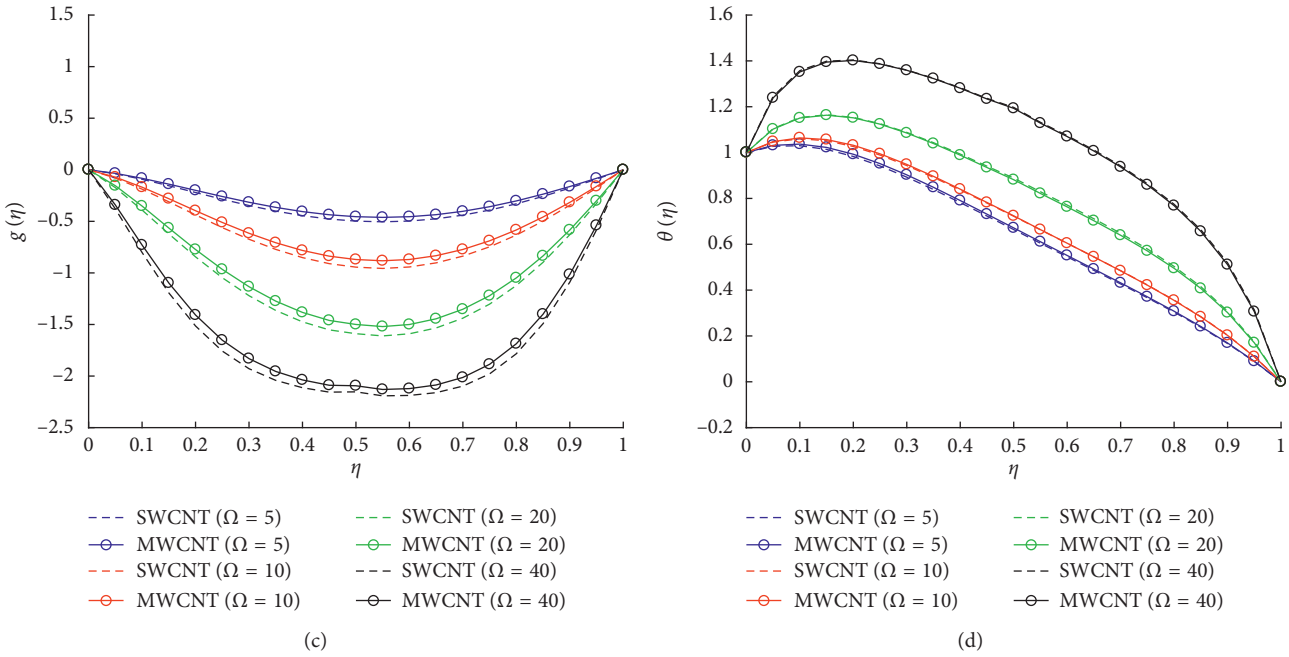


FIGURE 4: Effects of the rotation parameter, on the velocity and temperature profiles when $\phi = \mathrm{Ec} = \mathrm{Ec}_x = 0.1$, $\mathrm{Pr} = 6.2$, $A = S = 0.5$, and $R = 0$, taking $r = 5$ and $J = 2$.

nanoparticles (20 percent case) would not provide that much difference in comparison to the lower percentage nanofluid flow. In some practical applications, this issue can be useful when the nanoparticles are expensive or when adding more of them is causing some side problems.

Effect of rotational parameter $\Omega$ on the $y$ axis velocity is highlighted in Figure 4(a). When we raise the rotational parameters, there is a dual behavior for the $f(\eta)$. Near the lower wall, increasing the rotational parameter causes a decrease in the $y$ component velocity. However, there is a reverse trend for the vicinity of the upper wall. Figure 4(b) depicts the change in velocity in the $x$ direction by increasing the $\Omega$ value. There is a direct relationship between the increasing $\Omega$ value and the value of $x$-directional velocity in the core (far from the two walls). On the contrary, one can see the reverse trend for $0 < \eta < 0.3$ and $0.8 < \eta < 1.0$. Moreover, as it can be expected, the absolute values of rotational velocity increase by raising the rotational parameter (Figure 4(c)). By evaluating all the three mentioned regions in Figures 4(b) and 4(c), it can be concluded that effect of the rotational parameter on the SWCNTs are higher than MWCNTs. In Figure 4(d), we see the direct effect of the rotational parameter on the temperature profile, while the upper plate is moving toward the lower one.

To study the effect of the suction parameter $A$ on the velocity and temperature profiles, the value of the suction parameter increased from 0.5 to 2 by an increment of 0.5. Based on the obtained results in Figure 5, as it can be predicted easily, one can see that an increase in $A$ increases the velocity in the $y$ direction. It is crystal clear that the increase in $y$-directional velocity near the stationary wall would be maximum due to the suction at the lower wall. By getting closer to the moving wall, the effect of the suction parameter would be recessive. For the $x$-directional velocity profile, there is a reverse relationship between the $A$ and $f'(\eta)$ values. Moreover, a decrease in the $x$-directional velocity can lead to flow reversal in the center of the domain. Figure 5(c) illustrates the effect of the suction parameter on the rotational velocity. As it can be seen, by increasing the $A$ value from 0.5 to 2, the absolute value of rotational velocity increased and amount of increase in the SWCNTs is higher than MWCNTs due to their lower densities. The last picture of the Figure 5 resulted by changing the $A$ value and studying its effect on the temperature profile by keeping other parameters fixed. As it can be predicted easily, near the lower plate the temperature profile would be higher because of the suction source that we have in the bottom of the geometry. By moving toward the upper plate, the effect of the suction parameter will be weakened and the temperature profile will drop. The temperature profile for the solution which contains SWCNT will be higher compared to the MWCNTs nanofluid due to the higher thermal conductivity of the SWCNTs.

For the analysis of the variation of the squeezing number and its effect on the velocity and temperature profile, a series of Figure 6 are plotted. Based on the results in Figures 6(a)–6(d), there is a direct relationship between the squeeze number $S$ and the velocity profile in the $y$ direction when we compress the fluid between the plates (Figure 6(a)). The mentioned trend is opposite in the decompression period (Figure 6(b)). We are witnessing the same behavior as mentioned for $y$-directional velocity for $f'(\eta)$ values by changing the squeezing number; however, for the $x$-directional velocities, maximum changes occur close to the

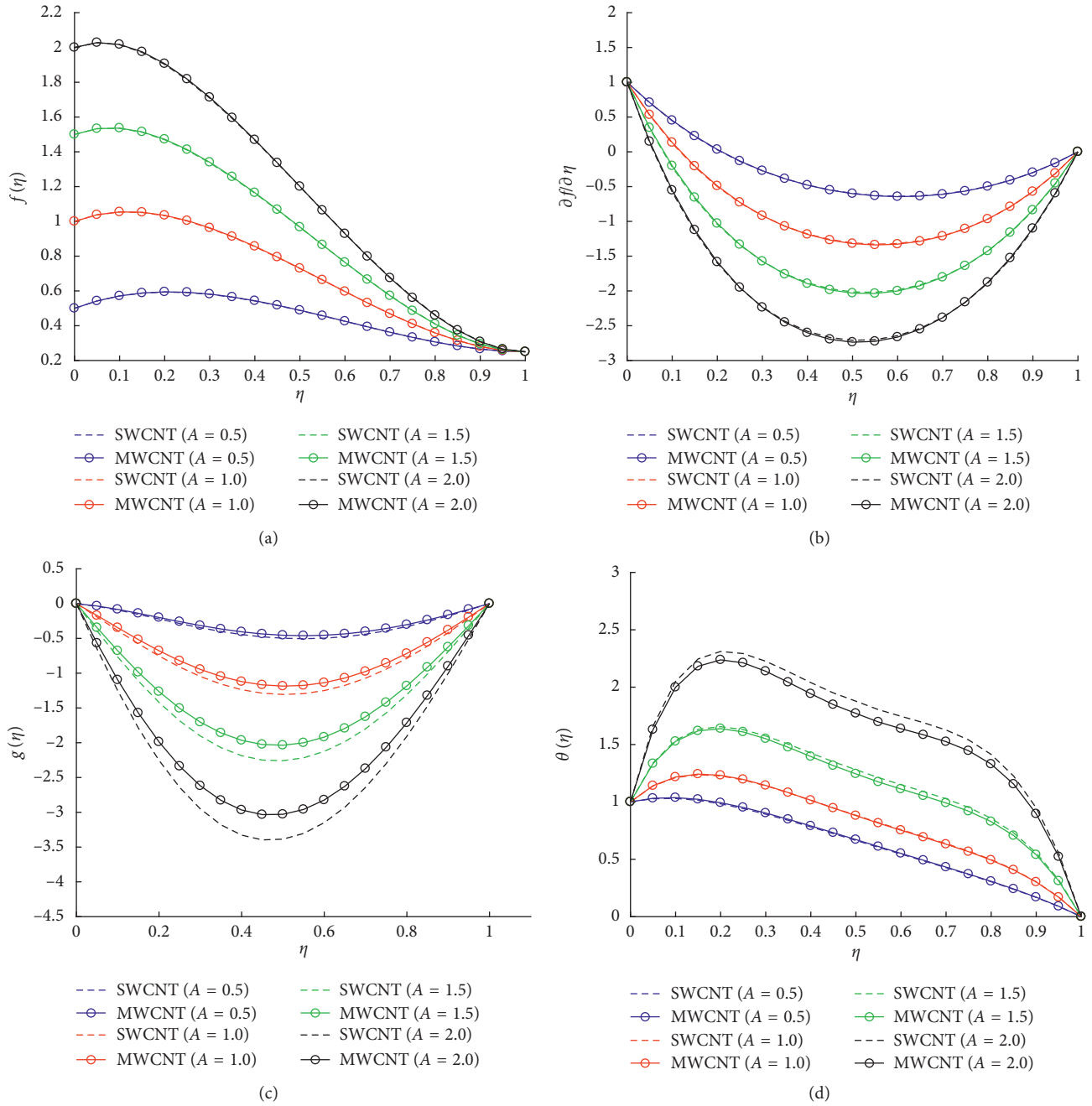


FIGURE 5: Effects of the suction parameter on the velocity and temperature profiles when $\phi = \mathrm{Ec} = \mathrm{Ec}_x = 0.1$, $\mathrm{Pr} = 6.2$, $\Omega = 5$, $S = 0.5$, and $R = 0$, taking $r = 5$ and $J = 2$.

center of the channel. Effect of the squeezing number on the rotational velocity is shown in Figures 6(e) and 6(f) for the compression and decompression cases. As we saw in previous parts, the effect of the squeezing number on the SWCNTs is higher than MWCNTs. It is worth to mention that when the upper wall is moving apart ($S < 0$), the effect of reverse flow in the center of the channel can be seen (Figures 6(d)–6(f)). Finally, one of the important analysis that we can have by the variation of the squeezing number is the change in the temperature profile. It is interesting that, by compression or decompression of the nanofluid, the temperature profile between them will increase. In the compression case, the solution with MWCNT is experiencing a relatively higher change; however, in the decompression mode, more changes in the temperature profile in the fluid with SWCNTs (Figures 6(g) and 6(h)) are obvious.

As it is obvious and discussed previously, by increasing the heat transfer rate, the temperature profile will drop. Different methods exist to raise the rate of heat transfer including adding nanoparticles and changing the squeezing number. One of the other methods of increasing the heat

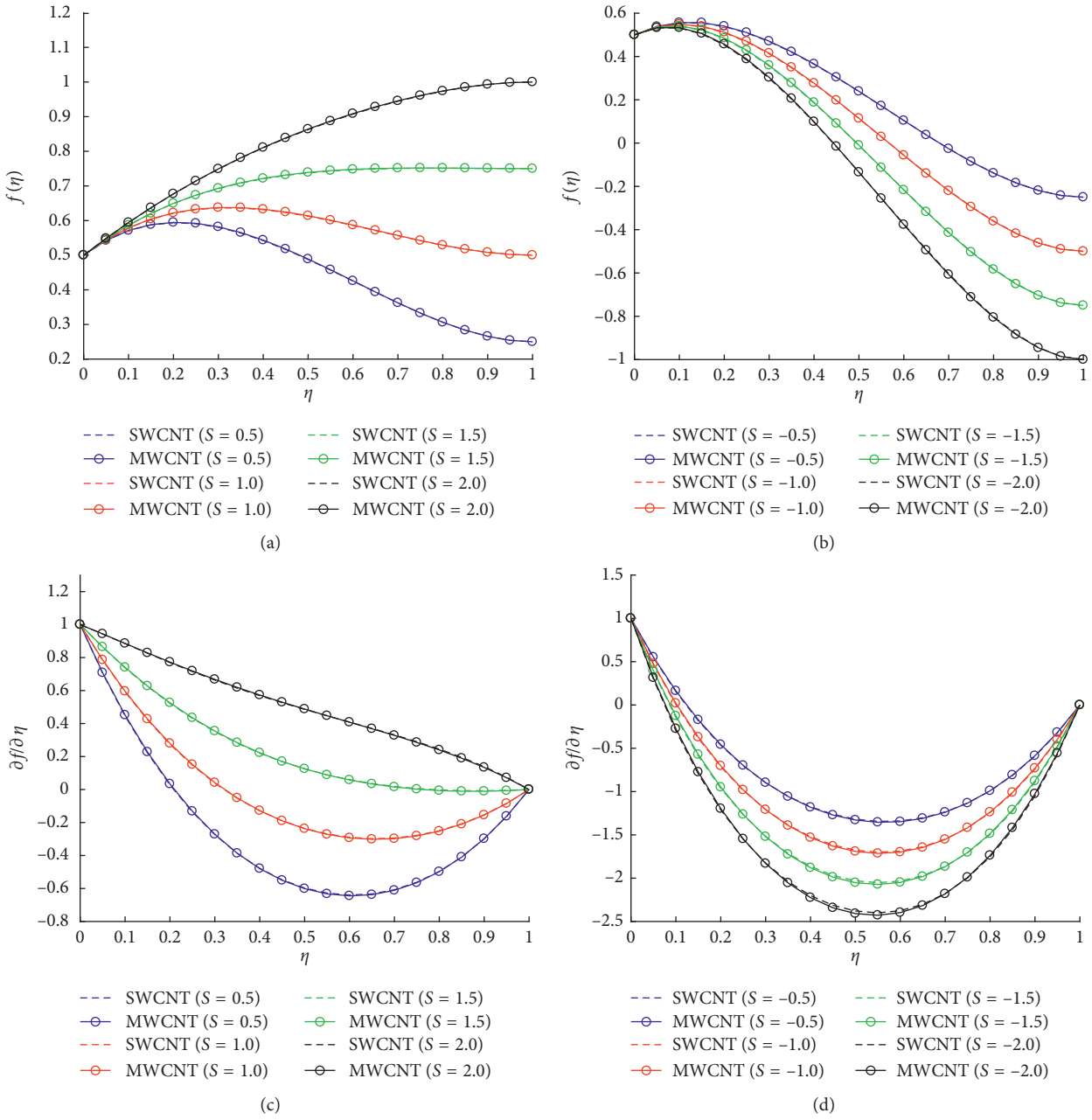


Figure 6: Continued.

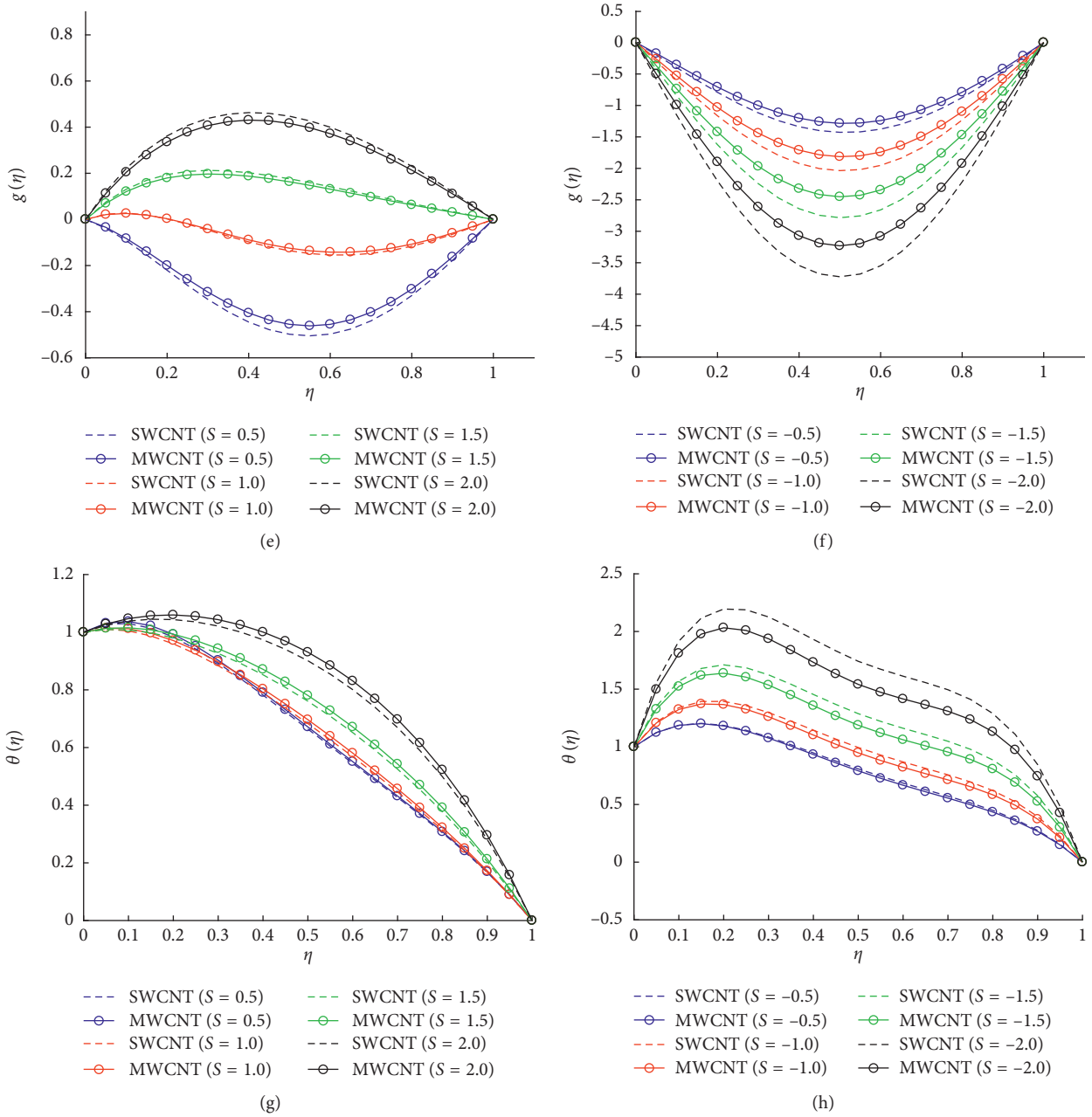


FIGURE 6: Effects of the squeezing number ($S$) on the velocity and temperature profiles when $\phi = \mathrm{Ec} = \mathrm{Ec}_x = 0.1$, $\mathrm{Pr} = 6.2$, $\Omega = 5$, $A = 0.5$, and $R = 0$, taking $r = 5$ and $J = 2$.

transfer rate for our geometry is increasing the radiation parameter. Figure 7(a) shows this matter when the upper wall is moving toward the stationary lower one. As it has shown, increasing the radiation parameter has helped to drop the temperature profile which is an indicator of more heat transfer. By taking a closer look into the obtained results, we see that, for the SWCNT case, we have more temperature drop which has caused higher thermal conductivity of this type of nanotubes. Also, Figure 7(b) illustrates the change of the Nusselt number by the $R$ value for both lower and upper plates, and the same mentioned trend is visible for the Nusselt number. Figure 8 compares the effect of different kinds of nanotubes, concentration, and squeezing number on the Nusselt number and skin friction coefficient. One can see in Figures 8(a) and 8(b) that increasing the concentration helps to have more heat transfer rate and bigger Nusselt number. Also, the variation of squeezing number changes the rate of heat transfer and Nusselt number. At the lower wall, increasing the value of $S$ causes an increase in the Nusselt number; however, this relationship is reversed for the upper wall. Moreover, the SWCNTs are mostly affected more with these variations of $S$ and $\phi$ values due to their higher thermal conductivities. Analysis of the deviation in the skin friction coefficient can

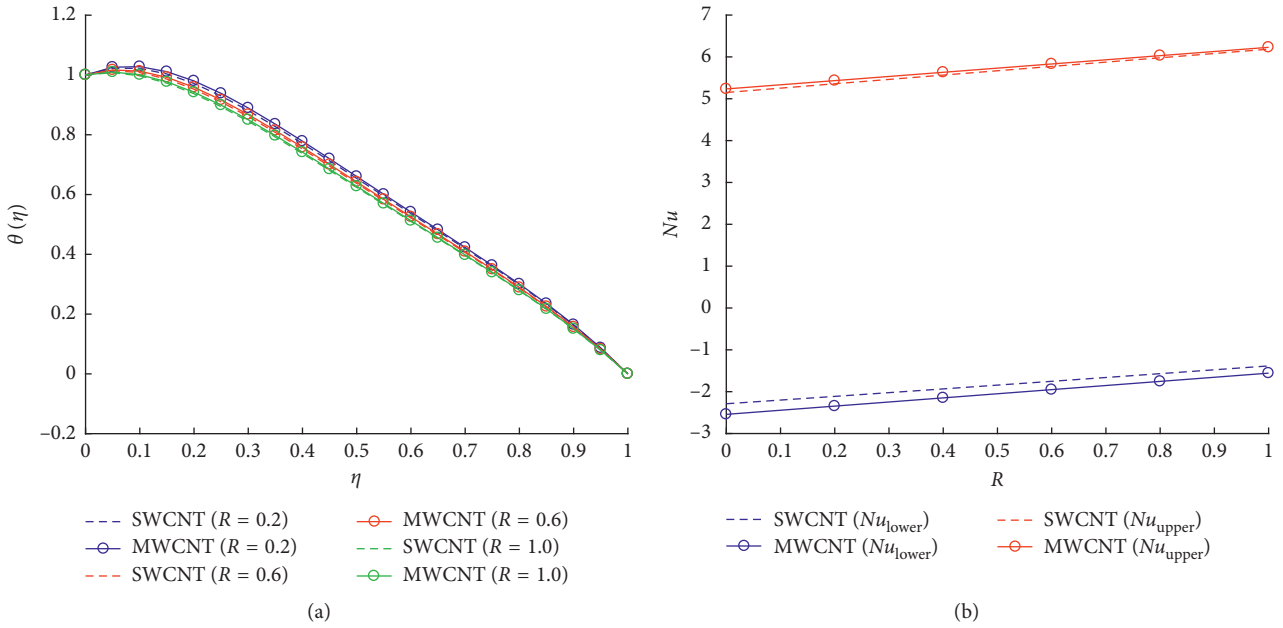


FIGURE 7: Effects of the $R$ value on the temperature profile and Nusselt number when $\phi = \mathrm{Ec} = \mathrm{Ec}_x = 0.1$, $\mathrm{Pr} = 6.2$, $\Omega = 5$, $A = 0.5$, and $S = 0.5$, taking $r = 5$ and $J = 2$.

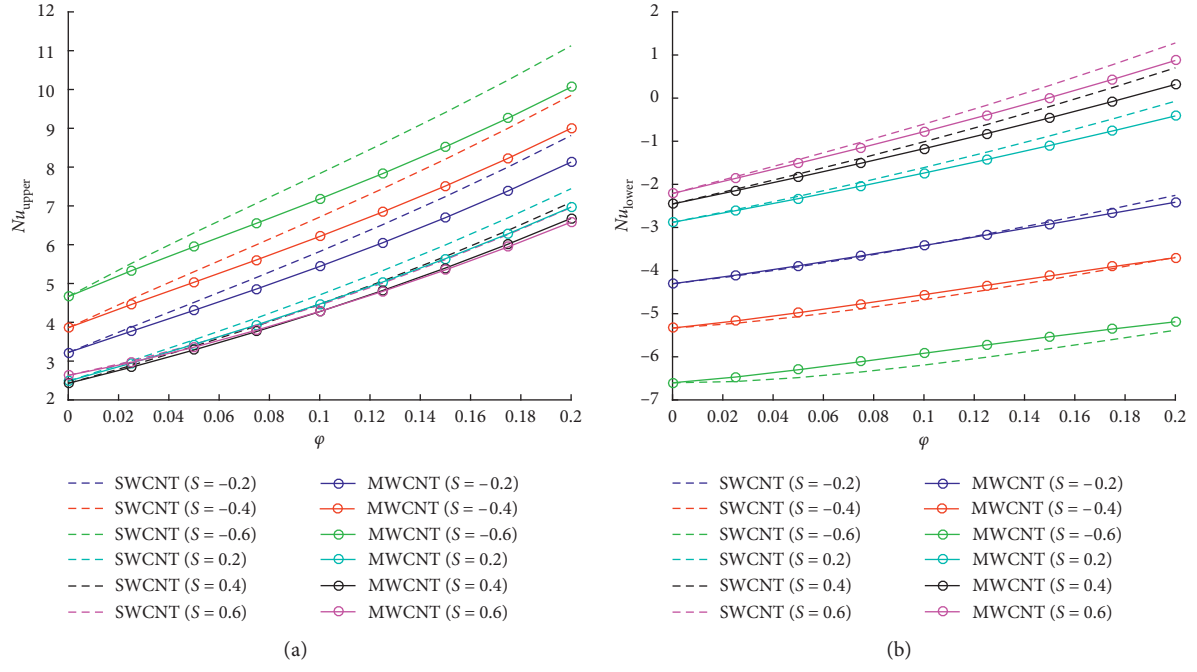


FIGURE 8: Continued.

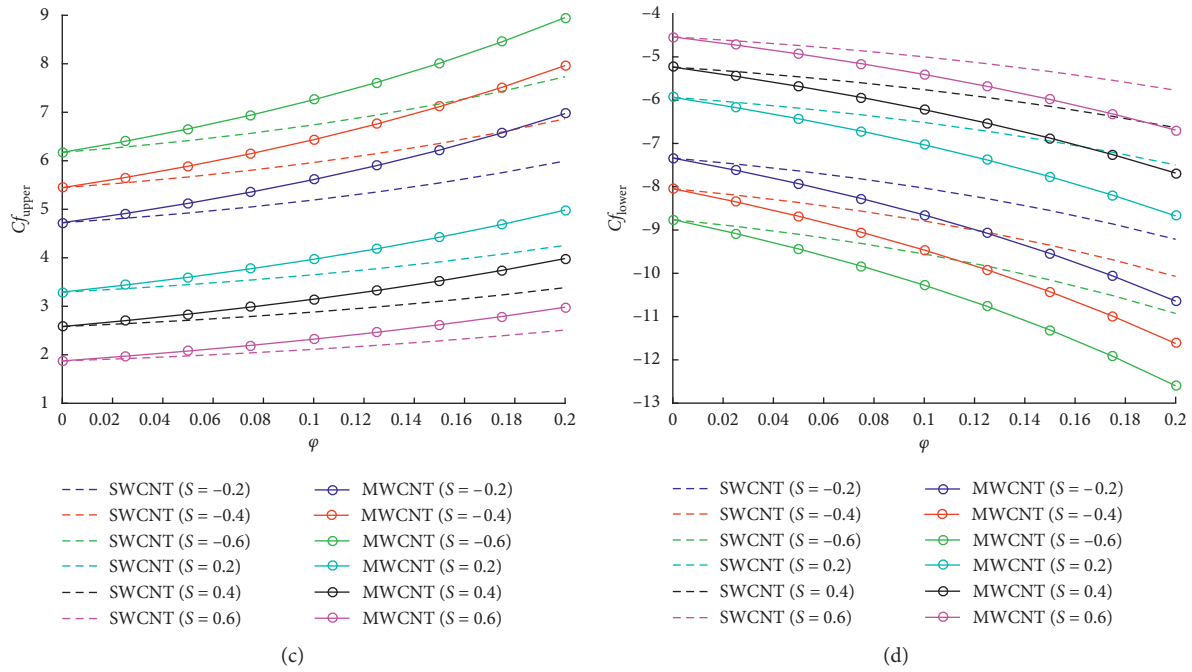


FIGURE 8: Effects of the squeezing number and concentration on the Nusselt number and skin friction coefficient when $\mathrm{Ec} = \mathrm{Ec}_x = 0.1$, $\mathrm{Pr} = 6.2$, $\Omega = 5$, and $A = 0.5$, taking $r = 5$ and $J = 2$.

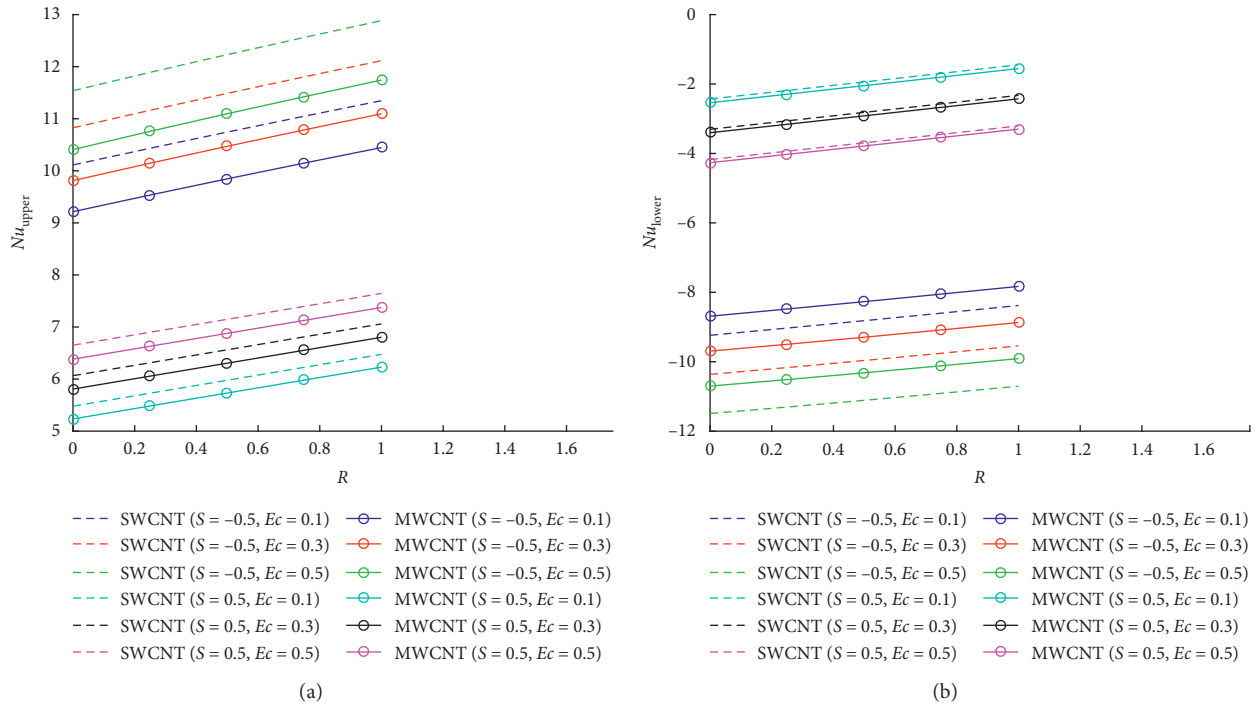


FIGURE 9: Effects of the Eckert number on the Nusselt number in the presence of $S$ and $R$ values when $\phi = \mathrm{Ec}_x = 0.1$, $\mathrm{Pr} = 6.2$, $\Omega = 5$, and $A = 0.5$, taking $r = 5$ and $J = 2$.

be found in Figures 8(c) and 8(d). For the upper wall in the geometry, increasing the nanoparticle volume fraction yields higher skin friction coefficient for both types of particles; however, squeezing number plays an opposite role and causes a downfall in the Cf values. We see a completely different trend for the values of the skin friction coefficient in the lower plate by changing the $\phi$ and $S$ parameters. By scrutinizing the Figures 8(c) and 8(d), it can be concluded

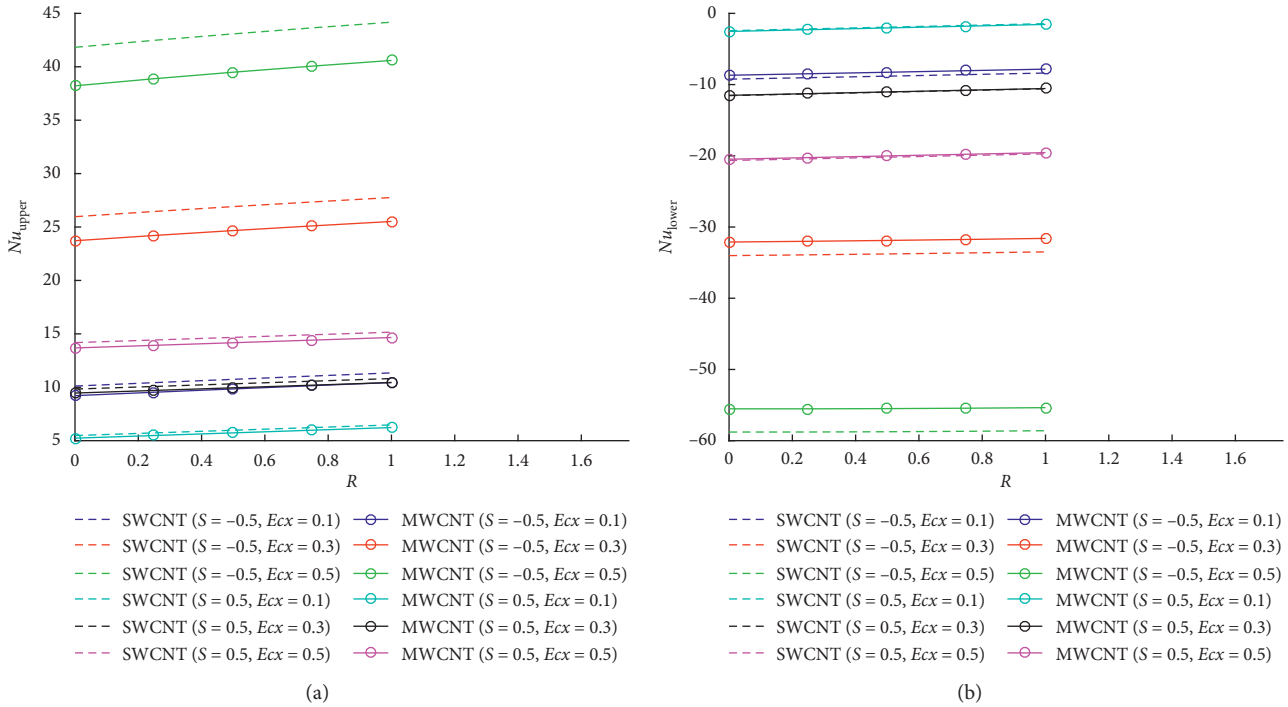


FIGURE 10: Effects of the modified Eckert number on the Nusselt number in the presence of $S$ and $R$ values when $\phi = \mathrm{Ec} = 0.1$, $\mathrm{Pr} = 6.2$, $\Omega = 5$, and $A = 0.5$, taking $r = 5$ and $J = 2$.

that Cf values corresponding to MWCNT's are higher on the upper wall and SWCNTs are taking higher values for the lower plate due to the difference in their densities.

The Eckert number Ec shows the relationship between kinetic energy of the flow and enthalpy difference across the thermal boundary layer. For characterizing the heat dissipation phenomena, the effects of changing the Eckert number in the presence of the radiation parameter are shown in Figures 9(a) and 9(b) for both upper and lower plates. In the upper plate, increasing the Eckert number has a direct effect on the rate of heat transfer and Nusselt number for both the compression $S > 0$ and decompression $S < 0$ cases. On the contrary, increasing the Ec values causes a downfall in the Nusselt number at the lower plate of the channel for both $S > 0$ and $S < 0$ cases. There is an interesting point about the obtained results, and the effect of changing the nanoparticle type is more remarkable in the decompression period and upper plate.

At the end of this section, effects of the change in the modified Eckert number $\mathrm{Ec}_x$ and radiation parameter $R$ are depicted in Figures 10(a) and 10(b). The results of the simulations in the mentioned scale show that there is a direct relationship between the modified Eckert number and heat transfer rate at the upper plate. For the lower plate, one can see an opposite relationship between the Nu and $\mathrm{Ec}_x$.

## 6. Conclusion

Three-dimensional CNT-based nanofluid flow in the presence of radiation heat transfer was analyzed by a new multiscale method. The 3D squeezing flow modeled by a set of nonlinear ordinary differential equations was obtained by implementing similarity solutions on the governing equations. The acquired equations were solved by a Galerkin-based spectral element method with Wavelet basis in different scales. Values of $f''(0)$ and $g'(0)$ were compared with a verified method from the literature for different scenarios to validate the algorithm and code. After verification of the method, the effect of different parameters on the velocity and temperature profiles is analyzed. The results of the simulations show that one can reach higher values in the temperature profile using MWCNTs instead of SWCNTs when the walls are moving toward each other. Moreover, the velocity components in the compression mode increase with the nanoparticle volume fraction in both solutions.

## Data Availability

The raw/processed data are available from the corresponding author on a reasonable request.

## Conflicts of Interest

The authors declare that they have no conflicts of interest.

## References

[1] J. Engmann, C. Servais, and A. S. Burbidge, "Squeeze flow theory and applications to rheometry: a review," *Journal of Non-Newtonian Fluid Mechanics*, vol. 132, no. 1–3, pp. 1–27, 2005.

[2] C.-Y. Wang, "The squeezing of a fluid between two plates," *Journal of Applied Mechanics*, vol. 43, no. 4, pp. 579–583, 1976.

[3] E. A. Hamza and D. A. Macdonald, "A fluid film squeezed between two parallel plane surfaces," *Journal of Fluid Mechanics*, vol. 109, pp. 147–160, 1981.

[4] E. A. Hamza, "The magnetohydrodynamic effects on a fluid film squeezed between two rotating surfaces," *Journal of Physics D: Applied Physics*, vol. 24, no. 4, pp. 547–554, 1991.

[5] P. Singh, V. Radhakrishnan, and K. A. Narayan, "Squeezing flow between parallel plates," *Ingenieur-Archiv*, vol. 60, no. 4, pp. 274–281, 1990.

[6] S. Islam, H. Khan, I. A. Shah, and G. Zaman, "An axisymmetric squeezing fluid flow between the two infinite parallel plates in a porous medium channel," *Mathematical Problems in Engineering*, vol. 2011, Article ID 349803, 10 pages, 2011.

[7] J. D. Sherwood, "Squeeze flow of a power-law fluid between non-parallel plates," *Journal of Non-Newtonian Fluid Mechanics*, vol. 166, no. 5-6, pp. 289–296, 2011.

[8] S. U. S. Choi and J. A. Eastman, "Enhancing thermal conductivity of fluids with nanoparticles," in *Proceedings of the ASME International Mechanical Engineering Congress and Exposition*, pp. 99–105, ASME, San Francisco, USA, November 1995.

[9] S. K. Das, S. U. S. Choi, W. Yu, and T. Pradet, *Nanofluids: Science and Technology*, Wiley, Hoboken, NJ, USA, 2007.

[10] S. Kakaç and A. Pramuanjaroenkij, "Review of convective heat transfer enhancement with nanofluids," *International Journal of Heat and Mass Transfer*, vol. 52, no. 13-14, pp. 3187–3196, 2009.

[11] X.-Q. Wang and A. S. Mujumdar, "A review on nanofluids—part II: experiments and applications," *Brazilian Journal of Chemical Engineering*, vol. 25, no. 4, pp. 631–648, 2008.

[12] W. Daungthongsuk and S. Wongwises, "A critical review of convective heat transfer of nanofluids," *Renewable and Sustainable Energy Reviews*, vol. 11, no. 5, pp. 797–817, 2007.

[13] A. Mokmeli and M. Saffar-Avval, "Prediction of nanofluid convective heat transfer using the dispersion model," *International Journal of Thermal Sciences*, vol. 49, no. 3, pp. 471–478, 2010.

[14] H. R. Rayatzadeh, M. Saffar-Avval, M. Mansourkiaei, and A. Abbassi, "Effects of continuous sonication on laminar convective heat transfer inside a tube using water-$TiO_2$ nanofluid," *Experimental Thermal and Fluid Science*, vol. 48, pp. 8–14, 2013.

[15] K. Khanafer, K. Vafai, and M. Lightstone, "Buoyancy-driven heat transfer enhancement in a two-dimensional enclosure utilizing nanofluids," *International Journal of Heat and Mass Transfer*, vol. 46, no. 19, pp. 3639–3653, 2003.

[16] S. S. Nourazar, M. Hatami, D. D. Ganji, and M. Khazayinejad, "Thermal-flow boundary layer analysis of nanofluid over a porous stretching cylinder under the magnetic field effect," *Powder Technology*, vol. 317, pp. 310–319, 2017.

[17] S. H. Seyedi, B. N. Saray, and M. R. H. Nobari, "Using interpolation scaling functions based on Galerkin method for solving non-Newtonian fluid flow between two vertical flat plates," *Applied Mathematics and Computation*, vol. 269, pp. 488–496, 2015.

[18] S. H. Seyedi, B. Nemati Saray, and A. Ramazani, "On the multiscale simulation of squeezing nanofluid flow by a highprecision scheme," *Powder Technology*, vol. 340, pp. 264–273, 2018.

[19] S. Hadi Seyedi, "Multi-resolution simulation of flow in porous media using wavelet analysis," Master thesis, Amirkabir University of Technology—Tehran Polytechnic, Tehran, Iran, 2013.

[20] A. Dib, A. Haiahem, and B. Bou-said, "Approximate analytical solution of squeezing unsteady nanofluid flow," *Powder Technology*, vol. 269, pp. 193–199, 2015.

[21] A. K. Gupta and S. Saha Ray, "Numerical treatment for investigation of squeezing unsteady nanofluid flow between two parallel plates," *Powder Technology*, vol. 279, pp. 282–289, 2015.

[22] U. Khan, N. Ahmed, M. Asadullah, and S. Tauseef Mohyuddin, "Effects of viscous dissipation and slip velocity on two-dimensional and axisymmetric squeezing flow of Cu-water and Cu-kerosene nanofluids," *Propulsion and Power Research*, vol. 4, no. 1, pp. 40–49, 2015.

[23] Q. Z. Xue, "Model for thermal conductivity of carbon nanotube-based composites," *Physica B: Condensed Matter*, vol. 368, no. 1–4, pp. 302–307, 2005.

[24] N. Freidoonimehr, B. Rostami, M. M. Rashidi, and E. Momoniat, "Analytical modelling of three-dimensional squeezing nanofluid flow in a rotating channel on a lower stretching porous wall," *Mathematical Problems in Engineering*, vol. 2014, Article ID 692728, 14 pages, 2014.

[25] H. Shahmohamadi and M. M. Rashidi, "VIM solution of squeezing MHD nanofluid flow in a rotating channel with lower stretching porous surface," *Advanced Powder Technology*, vol. 27, no. 1, pp. 171–178, 2016.

[26] U. Khan, N. Ahmed, and S. T. Mohyud-Din, "Numerical investigation for three dimensional squeezing flow of nanofluid in a rotating channel with lower stretching wall suspended by carbon nanotubes," *Applied Thermal Engineering*, vol. 113, pp. 1107–1117, 2017.

[27] S. S. Ghadikolaei, K. Hosseinzadeh, and D. D. Ganji, "Investigation on three dimensional squeezing flow of mixture base fluid (ethylene glycol-water) suspended by hybrid nanoparticle ($Fe_3O_4$-Ag) dependent on shape factor," *Journal of Molecular Liquids*, vol. 262, pp. 376–388, 2018.

[28] S. S. Ghadikolaei, K. Hosseinzadeh, M. Hatami, D. D. Ganji, and M. Armin, "Investigation for squeezing flow of ethylene glycol ($C_2H_6O_2$) carbon nanotubes (CNTs) in rotating stretching channel with nonlinear thermal radiation," *Journal of Molecular Liquids*, vol. 263, pp. 10–21, 2018.

[29] H. C. Brinkman, "The viscosity of concentrated suspensions and solutions," *The Journal of Chemical Physics*, vol. 20, no. 4, p. 571, 1952.

[30] B. Alpert, G. Beylkin, D. Gines, and L. Vozovoi, "Adaptive solution of partial differential equations in multiwavelet bases," *Journal of Computational Physics*, vol. 182, no. 1, pp. 149–190, 2002.

[31] B. Alpert, G. Beylkin, R. Coifman, and V. Rokhlin, "Wavelet-like bases for the fast solution of second-kind integral equations," *SIAM Journal on Scientific Computing*, vol. 14, no. 1, pp. 159–184, 1993.

[32] B. N. Saray and J. Manafian, "Sparse representation of delay differential equation of pantograph type using multi-wavelets galerkin method," *Engineering Computations*, vol. 35, no. 2, pp. 887–903, 2018.

[33] B. N. saray, "An efficient algorithm for solving Volterra integro-differential equations based on Alpert's multi-wavelets Galerkin method," *Journal of Computational and Applied Mathematics*, vol. 348, pp. 453–465, 2019.

[34] B. N. Saray, M. Lakestani, and C. Cattani, "Evaluation of mixed Crank–Nicolson scheme and Tau method for the solution of Klein–Gordon equation," *Applied Mathematics and Computation*, vol. 331, pp. 169–181, 2018.

[35] J. S. Geronimo and F. Marcellán, "On Alpert multiwavelets," *Proceedings of the American Mathematical Society*, vol. 143, no. 6, pp. 2479–2494, 2015.

[36] A. S. Butt and A. Ali, "Analysis of entropy generation effects in unsteady squeezing flow in a rotating channel with lower stretching permeable wall," *Journal of the Taiwan Institute of Chemical Engineers*, vol. 48, pp. 8–17, 2015.